The Astrophysical Journal Letters, 971:L35 (8pp), 2024 August 20 https://doi.org/10.3847/2041-8213/ad68fa

Observation of a Fully-formed Forward–Reverse Shock Pair due to the Interaction between Two Coronal Mass Ejections at 0.5 au

Domenico Trotta[1], Andrew P. Dimmock[2], Xochitl Blanco-Cano[3], Robert J. Forsyth[1], Heli Hietala[4], Naïs Fargette[1], Andrea Larosa[5], Noé Lugaz[6], Erika Palmerio[7], Simon W. Good[8], Juska E. Soljento[8], Emilia K. J. Kilpua[8], Emiliya Yordanova[2], Oreste Pezzi[5], Georgios Nicolaou[9], Timothy S. Horbury[1], Rami Vainio[10], Nina Dresing[10], Christopher J. Owen[9], and Robert F. Wimmer-Schweingruber[11]

[1] The Blackett Laboratory, Department of Physics, Imperial College London, London SW7 2AZ, UK; d.trotta@imperial.ac.uk
[2] Swedish Institute of Space Physics, 751 21 Uppsala, Sweden
[3] Departamento de Ciencias Espaciales, Instituto de Geofísica, Universidad Nacional autónoma de México, Ciudad Universitaria, 04150 Ciudad de México, Mexico
[4] Department of Physics and Astronomy, Queen Mary University of London, London E1 4NS, UK
[5] Istituto per la Scienza e Tecnologia dei Plasmi (ISTP), Consiglio Nazionale delle Ricerche, I-70126 Bari, Italy
[6] Space Science Center, University of New Hampshire, Durham, NH 03824, USA
[7] Predictive Science Inc., San Diego, CA 92121, USA
[8] Department of Physics,University of Helsinki, FI-00014 Helsinki, Finland
[9] Department of Space and Climate Physics, Mullard Space Science Laboratory, University College London, Dorking RH5 6NT, UK
[10] Department of Physics and Astronomy, University of Turku, FI-20014 Turku, Finland
[11] Institute of Experimental and Applied Physics, Kiel University, D-24118 Kiel, Germany
Received 2024 April 26; revised 2024 July 29; accepted 2024 July 30; published 2024 August 13

Abstract

We report direct observations of a fast magnetosonic forward–reverse shock pair observed by Solar Orbiter on 2022 March 8 at the short heliocentric distance of 0.5 au. The structure, sharing some features with fully-formed stream interaction regions, is due to the interaction between two successive coronal mass ejections (CMEs), never previously observed to give rise to a forward–reverse shock pair. The scenario is supported by remote observations from extreme ultraviolet cameras and coronagraphs, where two candidate eruptions compatible with the in situ signatures have been found. In the interaction region, we find enhanced energetic particle activity, strong nonradial flow deflections, and evidence of magnetic reconnection. At 1 au, well radially aligned Wind observations reveal a complex event, with characteristic observational signatures of both stream interaction region and CME–CME interaction, thus demonstrating the importance of investigating the complex dynamics governing solar eruptive phenomena.

Unified Astronomy Thesaurus concepts: The Sun (1693); Solar coronal mass ejections (310); Heliosphere (711); Interplanetary shocks (829)

1. Introduction

The Sun is an active star, responsible for generating a highly complex and dynamic environment in its surroundings, namely, the heliosphere. The solar activity and global field structures manifest themselves in a broad range of temporal and spatial scales in the heliosphere.

The most common global structures that strongly influence the heliosphere are stream interaction regions (SIRs) and coronal mass ejections (CMEs). Understanding their origin and propagation is pivotal for a broad range of applications. Such phenomena play an important role in the production of energetic particles and in the overall heliosphere energetics (Rice et al. 2003). SIRs and CMEs also represent major drivers of the Sun–Earth interaction, making their investigation crucial from a space weather perspective (Temmer 2021).

SIRs form when the fast solar wind emerging from solar coronal holes interacts with the slow solar wind upstream of it (see Richardson 2018 for a review). SIRs are crucial for planetary space weather (Zhang et al. 2007) and are the main source of heliospheric suprathermal particles at solar minimum. SIRs are characterized by a region of compressed plasma, bounded by a pair of forward–reverse pressure waves, which can steepen into forward–reverse shocks, traveling away from and toward the Sun in the solar wind rest frame, respectively (Belcher 1971). At 1 au, it was shown that less than 1% of the SIRs are associated with forward–reverse shock pairs (Jian et al. 2006), with even fewer observations in the inner heliosphere below 1 au, as shown by earlier Helios observations (Schwenn 1996).

CMEs are the largest eruptive events from the Sun, defined as an observable change in the coronal structure and an outward motion away from the solar atmosphere (Schwenn 1996). They propagate at large heliocentric distances, and their rate is proportional to solar activity. CMEs are excellent systems of energy conversion, from the release of magnetic energy at their origin to the shock-mediated conversion bulk flow energy into heat and energetic particles during their propagation (Chen 2011). In situ, CMEs show characteristic observable signatures and are often separated in a forward shock (not always present), a compressed sheath region, and magnetic ejecta (Kilpua et al. 2017).

Increased solar activity introduces the opportunity to study the interaction between multiple CMEs, which may happen in a variety of ways with different in situ signatures (see Lugaz et al. 2017 for a review). Multiple-CME events may lead to intense geomagnetic storms (Scolini et al. 2020) and extremely intense solar energetic particle (SEP) events (Zhuang et al. 2020). Interacting CMEs are the object of flourishing scientific

debate, establishing their role in heliospheric energetics (Lugaz & Farrugia 2014; Palmerio et al. 2021a). Forward–reverse shock pairs due to transient disturbances and CMEs were also reported at 1 au using early International Sun-Earth Explorer (ISEE) observations (Gosling et al. 1988).

The Sun is approaching the maximum activity of solar cycle 25, and novel data sets are now available, due to the groundbreaking Parker Solar Probe (PSP; Fox et al. 2016) and Solar Orbiter (Müller et al. 2020) missions. Thus, a novel observational window for solar eruptive phenomena has opened (e.g., Dresing et al. 2023).

In this work, we exploit this new window by reporting, for the first time, a fully-formed forward–reverse shock pair driven by two interacting CMEs at short heliocentric distances. The shock pair is observed by Solar Orbiter as close to the Sun as 0.5 au on 2022 March 8. The Sun was particularly active when the event took place, and we identified two candidate CMEs originating on March 6 and 7 from the active regions (ARs) 12957 and 12958, by combining solar disk, coronagraph, and heliospheric imagery from the Solar Terrestrial Relations Observatory Ahead (STEREO-A; Kaiser et al. 2008). These observations were complemented with near-Earth remote observations from the Solar Dynamics Observatory (SDO; Pesnell et al. 2012) and the Solar and Heliospheric Observatory (SOHO; Domingo et al. 1995). Finally, we study the evolution of the shock pair using direct observations from the radially well-aligned Wind (Ogilvie & Desch 1997) spacecraft at 1 au. We describe the data products used in Section 2, while the results are presented in Section 3, and the conclusions reported in Section 4.

2. Data

For remote-sensing observations, we use STEREO-A's Sun Earth Connection Coronal and Heliospheric Investigation (SECCHI; Howard et al. 2008) suite, with focus on the Extreme Ultraviolet Imager (EUVI) observing the solar disk, the COR2 coronagraph, imaging the solar atmosphere up to 15 $R_\odot$, and the Heliospheric Imager (HI) cameras, observing the heliosphere in the elongation range 4°–88°7. We complement these data with near-Earth observations from SDO (Pesnell et al. 2012), imaging the solar disk, and SOHO (Domingo et al. 1995), imaging the solar corona.

At Solar Orbiter, we use the fluxgate magnetometer (MAG; Horbury et al. 2020). Ion moments and suprathermal electron pitch angle distributions and composition are from the Solar Wind Analyser (SWA) suite (Owen et al. 2020). Energetic particles have been measured by the Energetic Particle Detector (EPD; Rodríguez-Pacheco et al. 2020).

From Wind, we use the Magnetic Field Investigation (MFI; Lepping et al. 1995) measurements. For Wind plasma measurements, we use data from the Solar Wind Experiment (SWE; Ogilvie et al. 1995), which we checked against data from the Three-Dimensional Plasma and Energetic Particle Investigation (3DP; Lin et al. 1995) instrument for ion moments.

3. Results

On 2022 March 8, Solar Orbiter crossed a forward–reverse shock pair at 0.49 au (Figure 1). The time separating the two shocks is 6 hr and 47 minutes.

Figure 1 shows an overview of the event, with the forward–reverse shock pair highlighted by the dashed magenta lines. The interaction region between the shocks is associated with magnetic field compression, two subsequent increases in the bulk flow speed, and enhanced total plasma pressure (see dashed and dashed–dotted lines in Figures 1(c), (d), and (f)). While the structure is reminiscent of a fully-formed SIR, we note unexpected profiles of some parameters, such as the hot, low-density interior. Furthermore, forward–reverse shock pairs at such short heliocentric distances are not consistent with any previous observations associated with SIR evolution, generally yielding forward–reverse shock pairs at 1 au and beyond (see, e.g., Richardson 2018).

A closer analysis of the event reveals that the forward–reverse shock pair is not driven by an SIR, where fast and slow solar wind interact. Rather, the forward–reverse shock pair is driven by the interaction between two CMEs (CME1 and CME2 in chronological order; see Figure 1) with different propagation speeds (about 290 and 450 km s^{-1}, respectively).

This is readily seen by the presence of several clear indicators of CME material (see Zurbuchen et al. 2016) both before and after the interaction region, including the smooth magnetic field rotations upstream/downstream of the interaction, the enhanced O^{7+}/O^{6+} ratios, and the bidirectional pitch angle distributions of suprathermal electrons (Figures 1(c), (h), and (i)). Figure 1 shows that CME1 is both slower (Figure 1(d)) and possibly magnetically less well connected to the Sun (less clear bidirectional electron signature).

The start of CME1, on 2022 March 7, 7:23:46 UT, magenta line in Figure 1, has not steepened into a shock due to the slow CME1 propagation speed. Downstream of the CME1 compressive wave, we observe a change of parameters (around 6:00 UT on March 8), marking the start of enhanced energetic particle fluxes within the CME1 ejecta (Figures 1(a) and (b)). Protons with energies of up to 7 MeV were found irregularly distributed within both the CME1 and CME2 ejecta and in the interaction region. This behavior may depend on the intrinsic complexity of the environment measured. Furthermore, complexity may be due to further injection of energetic particles at the Sun, where we identified a type III radio burst around 4:30 UT (not shown here).

The shock parameters, computed using the SerPyShock package (Trotta et al. 2022) and systematically changing the upstream/downstream averaging windows from a few seconds to 2 minutes, are summarized in Table 1. The forward shock is oblique ($\theta_{Bn} \sim 60°$), with small Mach numbers, while the reverse shock appears more perpendicular and stronger, compatible with previous studies of SIR shocks (Kilpua et al. 2015). Starting at about 13:00 UT, we report enhanced particle fluxes upstream of and well connected to the forward shock, readily seen at high energies in the spectrogram in Figure 1(g). This extended particle foreshock propagating in CME1 and thereby producing foreshock waves will be the object of further study addressing the shocks' small-scale behavior.

We focus on the interaction region properties, showing a zoom of the Solar Orbiter measurements together with a simplified sketch of the event in Figure 2. Note that the sketch assumes head-on interaction of the events, which may not be the case, as in Figure 3. The trailing part of the interaction region is characterized by higher plasma densities, lower temperatures, and higher elemental abundances (Figure 2(f)) than the leading portion. The pitch angle distributions show that magnetic connectivity changes in the end portion of the interaction region from field lines connected to the Sun at one

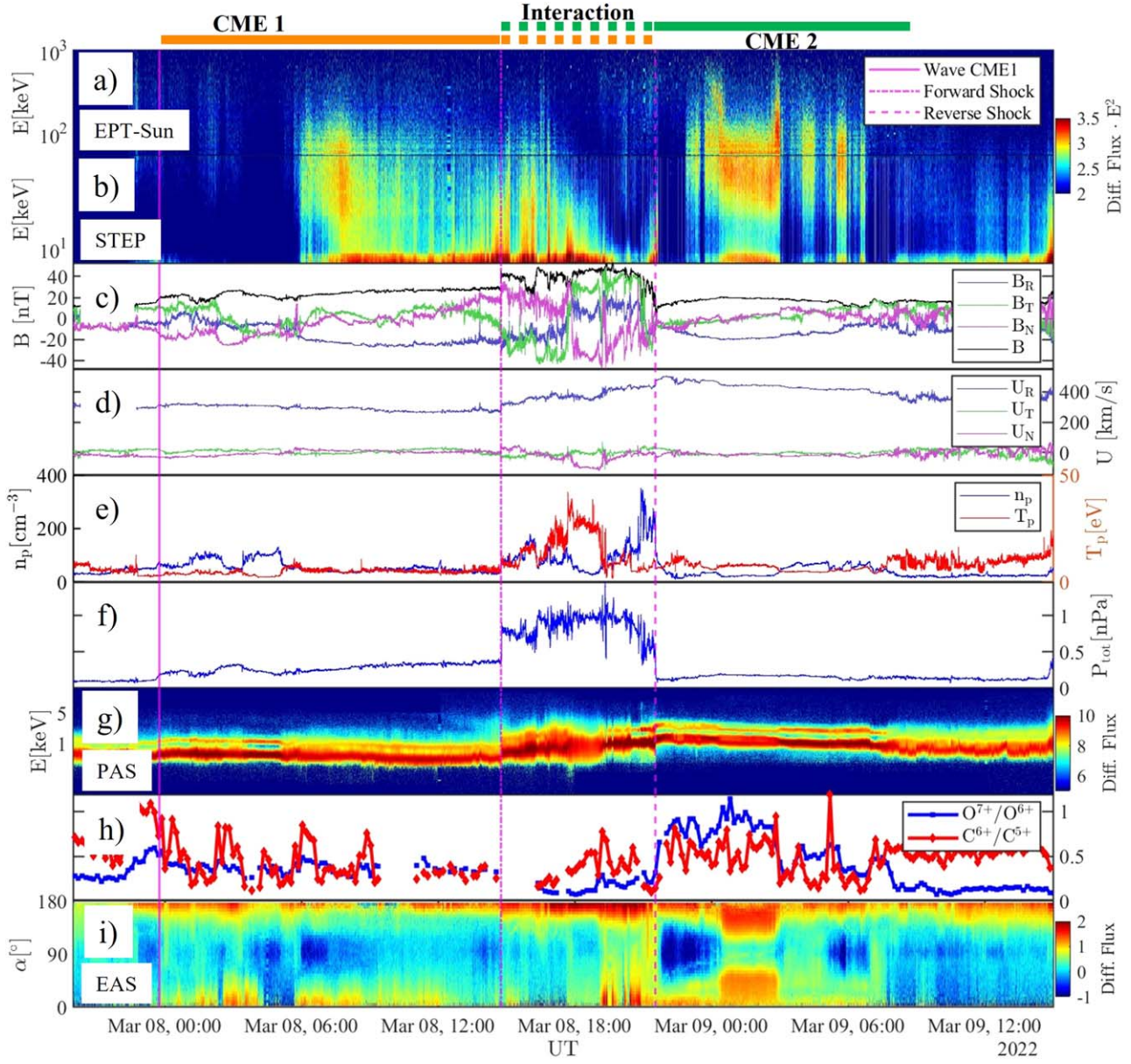

Figure 1. Summary of Solar Orbiter observations. Energetic ion differential fluxes (in $E^2 \cdot cm^{-2}\, s^{-1}\, sr^{-1}$ MeV) as measured by (a) EPD's Sun-directed Electron Proton Telescope (EPT) and (b)Supra Thermal Electron Proton (STEP) sensor. (c) MAG normal mode magnetic field magnitude and components in spacecraft-centered Radial–Tangential–Normal (RTN) coordinates (Fränz & Harper 2002). (d)–(e) Proton bulk flow speed, proton density, and temperature as measured by SWA Proton Alpha Sensor (PAS). (f) Plasma total pressure ($P_{tot} = n_p\, k_B\, T_p + \frac{B^2}{2\mu_0}$, where k_B and μ_0 are the Boltzmann constant and the vacuum magnetic permeability, respectively). (g) One-dimensional energy flux (in $cm^{-2} s^{-1}$ eV) measured by PAS. (h) Element abundance ratios measured by the SWA Heavy Ion Sensor (HIS). (i) Integrated pitch angle distributions for electrons with energies larger than 100 eV as measured by SWA Electron Analyser Sensor (EAS; in $cm^{-2}\, s^{-1}$ eV). The continuous, dashed–dotted and dashed lines show the times at which Solar Orbiter crosses the CME1 wave and the forward and reverse shocks, respectively.

end to those having both ends connected. These observations emphasize that the interaction region consists of plasma from two different sources.

The interaction region shows substructuring, with irregular behavior in many measured quantities (Figure 2, left). We suggest that this is due to the spacecraft probing, in rapid succession, the material at the end of CME1 and material in the CME2 sheath and cloud (Figure 2(h)), as is particularly evident in the plasma signatures (Figures 2(c) and (e)). Plasma belonging to different regions may mix due to reconnection, as discussed three paragraphs below.

The leading part of the interaction region is characterized by hot plasma, strongly processed by the forward shock. Progressing through the interaction, we observe abrupt changes in magnetic field direction, in association with strong transverse flow deflections (at 18:00 and 19:05 UT). These correspond to plasma being deflected away from the radial direction in the interaction between the two events, which may happen at an oblique angle, as further indicated by remote observations and Figure 3. We interpret this region as the interface between the two CMEs.

As done in observations of planar magnetic structures in the solar wind (e.g., Nakagawa et al. 1989) and in CME-driven sheath regions (Palmerio et al. 2016), we applied a Minimum Variance Analysis (MVA) to the magnetic field in the interaction region. In the interval from the immediate downstream of the

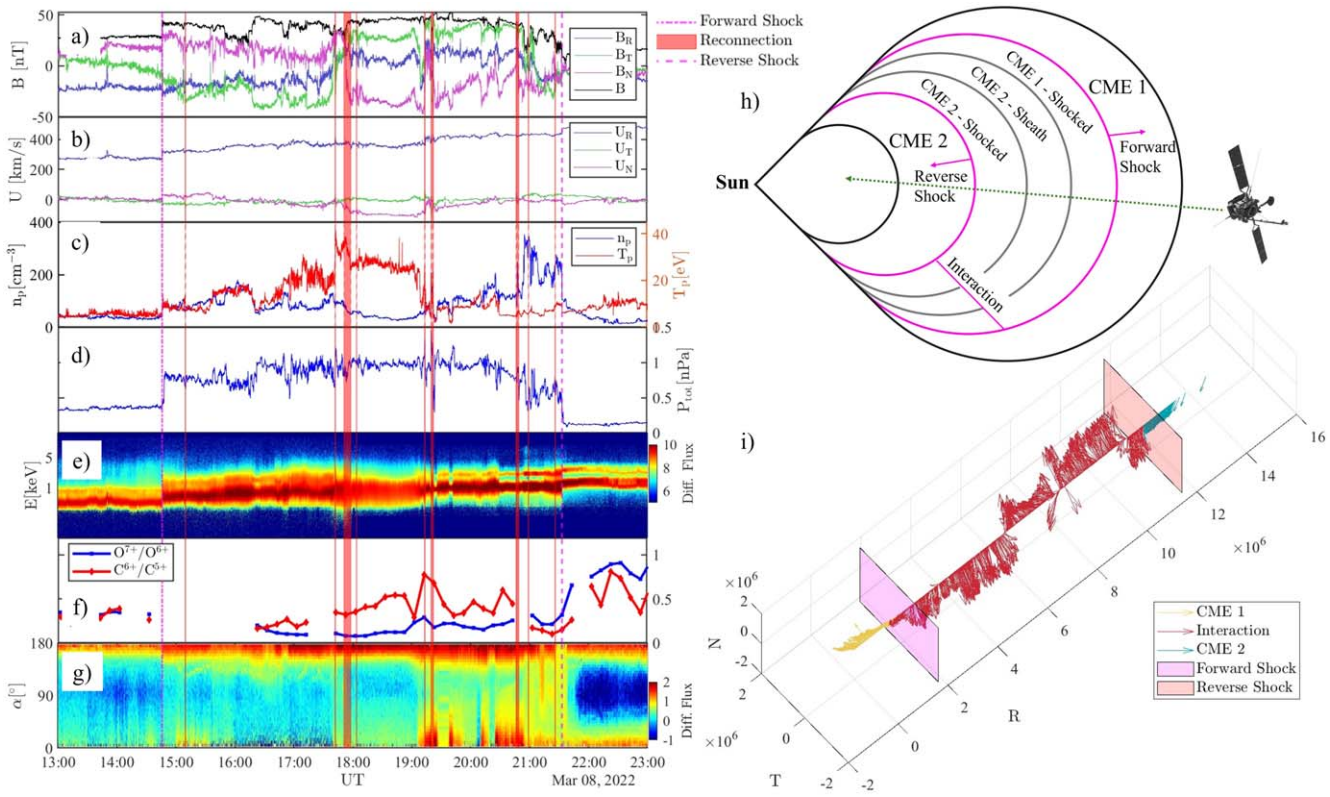

Figure 2. (a)–(g) Zoom on the interaction region as in Figure 1 without the energetic particles spectrogram. The vertical orange shaded regions correspond to reconnection exhaust crossings. (h) Simplified sketch representing the event assuming head-on interaction with the identified areas within the interaction and the Solar Orbiter trajectory (spacecraft model: https://www.esa.int/Science_Exploration/Space_Science/Solar_Orbiter). (i) Three-dimensional plot of magnetic field vectors in RTN for the event. Yellow, red, and blue arrows are measurements taken in CME1, interaction, and CME2 regions, respectively. The magenta/orange planes represent the forward–reverse shock pair.

Table 1
Shock Times and Parameters Inferred from Solar Orbiter Direct Observations

Shock	Time (UT)	$\langle \hat{n}_{RTN} \rangle$	$\langle \theta_{Bn} \rangle$ (deg)	$\langle r_B \rangle$	$\langle r \rangle$	$\langle v_{sh} \rangle$(km s^{-1})	β_{up}	M_{fms}	M_A
Forward	08-Mar-2022 14:04:26	[0.95-0.11 0.30]	59	1.5	2	367	0.09	1.2	1.1
Reverse	08-Mar-2022 21:33:01	[-0.94 0.15 0.32]	69	2	2.1	−373	3.1	2	3.8

Note. The parameters shown are (left to right): shock normal vector, θ_{Bn}, magnetic compression ratio r_B, gas compression ratio r, shock speed v_{sh}, upstream plasma beta β_{up}, fast magnetosonic, and Alfvénic Mach numbers (M_{fms} and M_A, respectively).

forward shock to the reverse shock, the intermediate-to-minimum eigenvalue ratio of the MVA matrix is large ($\lambda_2/\lambda_3 \sim 8$). This implies the existence of a well-defined minimum variance direction. Projecting the magnetic field components in the MVA frame highlights the change at the interface region at 18:00 UT mentioned above (not shown here). Strong changes at 19:00 UT are also found both with the MVA and magnetic reconnection diagnostics, indicating that there may be more than one interface crossing.

Further characterization was performed, searching for magnetic reconnection signatures, crucial for mixing plasmas efficiently (e.g., Russell et al. 1990). We used the magnetic reconnection method successfully applied to Solar Orbiter data in Fargette et al. (2023). Orange shaded regions in Figure 2 (left) correspond to reconnection exhaust crossings. It is readily seen that the interaction region undergoes strong reconnection activity, very long-lasting around 18:00 UT, corresponding to the previously identified CME–CME interface and corroborating the interpretation of complex mixing of CMEs.

Finally, in Figure 2(i) we show a three-dimensional plot of the magnetic field vectors as measured by Solar Orbiter in the CME1, interaction region, and CME2 intervals, with the forward–reverse shock pair represented as the magenta/orange planes, respectively. The interface between the two CMEs can be clearly seen in the sharp change of direction of the magnetic field.

The spacecraft orbital configuration during the event makes it possible to get unique insights about the evolution of this novel interaction structure. By combining solar disk, coronagraph, and heliospheric imagery from STEREO-A and near-Earth spacecraft, we identified two candidate eruptions from the Sun, possibly the progenitors of the observed interaction event. An overview of our findings is provided in Figure 3. CME1 appears as a faint event in STEREO-A imagery and is not visible in SOHO data, while CME2 can be observed in both views (Figures 3(a) and (b)). By performing reconstructions of both events using the Graduated Cylindrical Shell (GCS; Thernisien 2011) model, we find a propagation direction of (θ,

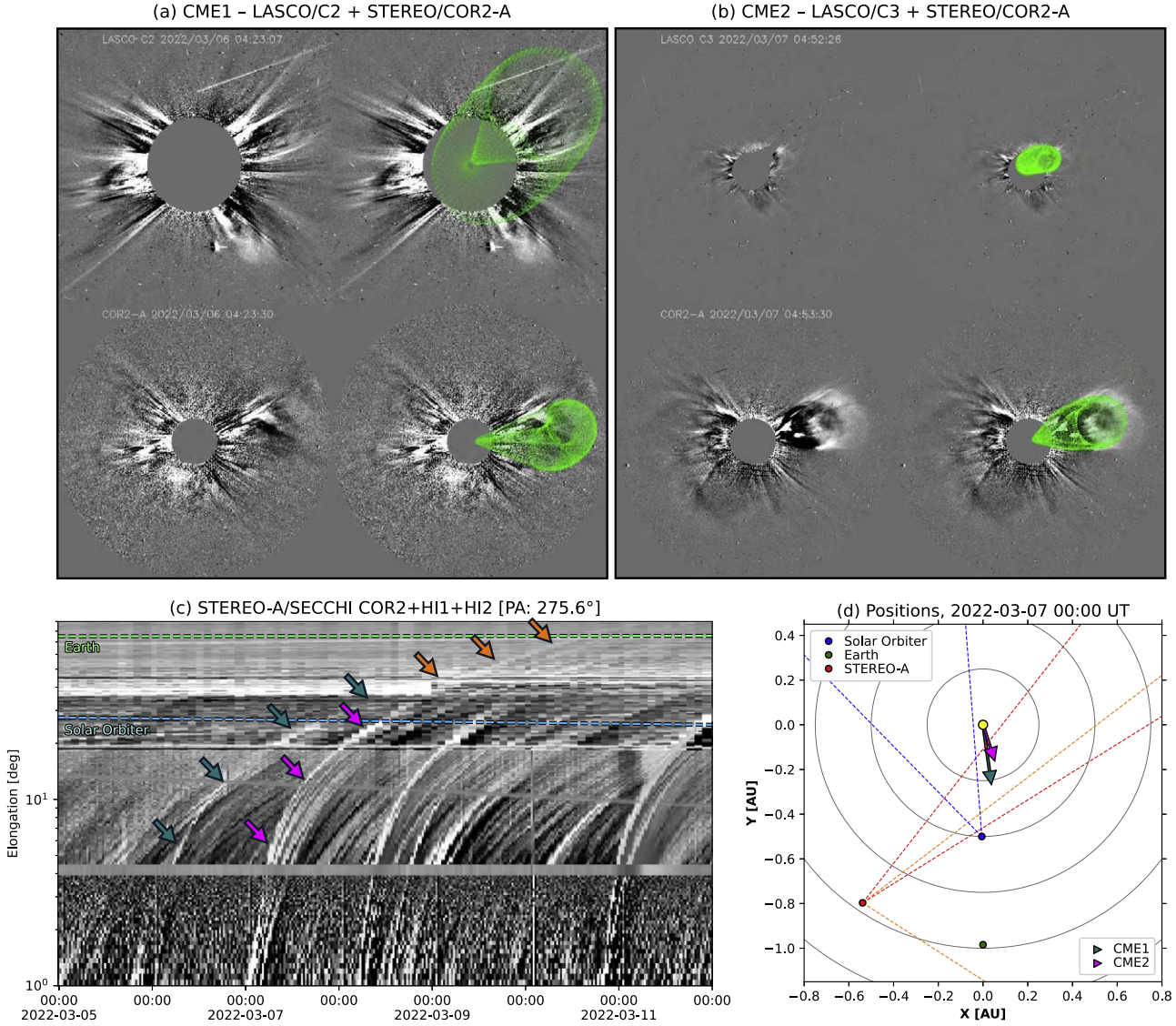

Figure 3. Overview of some available remote-sensing observations of the 2022 March CME–CME interaction event. Coronagraph observations of (a) CME1 and (b) CME2 from the (top) SOHO and (bottom) STEREO-A viewpoints. The rightmost panels show the GCS wireframe projected onto each plane-of-sky view. (c) Time–elongation map built using data from the COR2, HI1, and HI2 cameras on board STEREO-A. The tracks of CME1 and CME2 are indicated with teal and magenta arrows, respectively, and the combined track after interaction is shown by orange arrows. The time-dependent elongation angles of Solar Orbiter and Earth are highlighted via light blue and green dashed lines, respectively. (d) Orbit plot showing the relative positions of Solar Orbiter, Earth, and STEREO-A during 2022 March 7. The propagation directions of the two CMEs according to the GCS results are shown with arrows, while the dashed lines indicate the fields of view of the SoloHI (blue), HI1-A (red), and HI2-A (orange) heliospheric imagers.

Table 2
Summary of Remote Observations and GCS Fit Results for CME1 and CME2

CME	Time (UT)	θ (deg)	ϕ (deg)	Speed (km s^{-1})
1	06-Mar 00:00	−2	8	500
2	07-Mar 00:00	9	18	425

Note. The θ and ϕ angles are in Stonyhurst coordinates.

$\phi) = (-2°, 8°)$ for CME1 and $(\theta, \phi) = (9°, 18°)$ for CME2 in Stonyhurst coordinates, with speeds of $\sim$500 km s^{-1} and $\sim$425 km s^{-1}, respectively (summarized in Table 2). Such parameters indicate that the interaction between the two CMEs is not perfectly head-on, consistent with the tangential flow deflections found by means of direct observations at both Solar Orbiter and Wind, as in the Figure 4 discussion. We remark that the reconstruction for CME1 is performed using the STEREO-A viewpoint only and is thus associated with larger uncertainties (see, e.g., Verbeke et al. 2023). We note that CME1 is only slightly faster than CME2 according to GCS results, which is likely to lead to CME2 catching up with CME1 due to solar wind preconditioning (e.g., Temmer et al. 2017). The source region of CME1 is a stealth CME (see, e.g., Palmerio et al. 2021b) from AR 12957 around 00:00 UT on March 6 (mostly visible off the limb from STEREO-A), while CME2 is associated with a more energetic eruption from AR 12958 around 00:00 UT on March 7. We follow the interplanetary propagation of the two CMEs via time–elongation maps that employ STEREO/SECCHI data (Figure 3(c)), where the two CME tracks are seen to converge (possible indication of merging) beyond Solar Orbiter's heliocentric distance (see Figure 3(d) for the geometry of the STEREO/HI fields of view). We note that we do not find CME signatures in

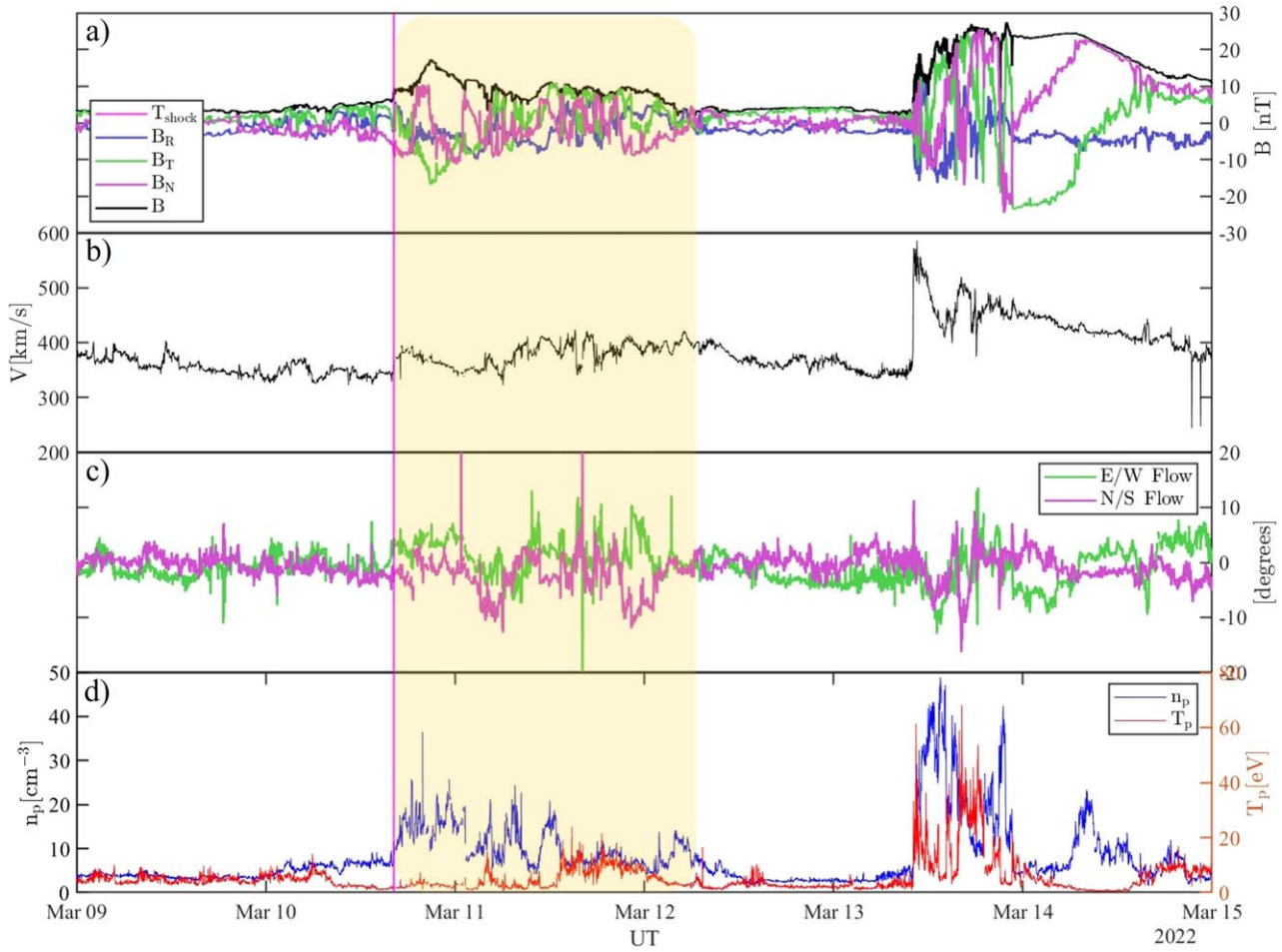

Figure 4. Wind observations of the event at 1 au (shaded area). From top to bottom: magnetic field magnitude and components in RTN (a), proton bulk flow speed and tangential flows ((b), (c)), protons density and temperature (d). The magenta line marks the forward shock crossing.

heliospheric images from SoloHI on board Solar Orbiter, consistent with the two CMEs originating from the western hemisphere (see Figure 3(d)). While identification of the remote counterparts of CME1 and CME2 is not straightforward, our analysis shows that both candidates are compatible with eruptions directed close to the Sun–Earth line and with their arrival time at Solar Orbiter. Such remote observations highlight how even "faint" solar eruptions can give rise to energetic events through complex interactions.

During the event, the Solar Orbiter–Earth longitudinal separation was about 9°. We exploited the configuration and found an in situ structure crossing the Wind spacecraft at the Sun–Earth Lagrange L1 point at 13:00 UT on 2023 March 10, compatible with the Solar Orbiter event propagating at about 400 km s^{-1} speed from 0.5 to 1 au.

In Figure 4, it is readily noted that the forward–reverse shock pair is not present at Wind. Only a fast-forward shock is observed at Wind ahead of the whole structure, crossing the spacecraft on March 10 at 16:11:32 UT. The shock has a complex magnetic structure in both the upstream and downstream regions, which probably dominates its small-scale evolution features (see Trotta et al. 2024). A data gap in plasma measurements immediately downstream makes shock parameter estimation particularly difficult. Nevertheless, we estimate that the shock is oblique ($\theta_{Bn} \sim 55°$) and the Alfvén Mach number is very low, close to 1.

The event at Wind is compatible with the complex ejecta resulting from the interaction of multiple CMEs, as reported in Lugaz et al. (2017), where characteristics of the individual "parent" eruptions can no longer be discerned. Transverse flow deflections are found at 1 au, also present in the 0.5 au observations. This indication of oblique interaction between the two CMEs is compatible with remote observations and the GCS fits discussed above (Figure 3). The structure at 1 au also has some features reminiscent of an SIR (e.g., magnetic compression), but is missing the typical fast stream signature corresponding to the reverse pressure wave. We note that the solar wind speed is slower in the first portion of the complex ejecta than in the second, thus maintaining the general trends of the structure observed at Solar Orbiter. It is also possible that the 10° separation between the two locations was sufficient to measure different parts of the event between Solar Orbiter and the Sun–Earth L1 point. Therefore, these joint observations highlight the transient nature of this novel interaction. The interaction has weakened from 0.5 to 1 au, as it can be seen in the 7 day overview plot in Figure 4, where the interaction appears as a very moderate event, quite common during solar maximum. This is particularly evident when compared with another CME event crossing Wind around 12:00 UT on March 13 (see Laker et al. 2024 for further details). Such behavior is in contrast with that expected from SIR-driven forward–reverse shock pairs that tend to get stronger as they move to larger heliocentric distances (Richardson et al. 2022). The event was

not found to cause any major space weather disturbance at Earth, consistent with the lack of periods with steady magnetic field orientations (Dimmock et al. 2019).

4. Conclusions

We reported direct observations of a fully-formed reverse–forward shock pair at the very low heliocentric distance of 0.5 au. While such a shock pair is typically associated with an SIR, it was found to be originated from the interaction between a fast and a slow CME. To our knowledge, this is the first time that such an observation is reported at such small heliocentric distances.

The CME–CME interaction drives a complex compression region, where the interface separates plasma from two different sources and is characterized by a high level of magnetic reconnection activity and several irregularities in the measured plasma conditions. Such characterization underlines the role of this structure in creating favorable conditions for efficient energy dissipation (Richardson 2018).

Energetic ions up to several MeV were observed, with a strongly irregular behavior, influenced by the complex plasma environment, stimulating an advancement of knowledge for energetic particle behavior in the heliosphere. On one hand, due to novel, high time-energy resolution of energetic particles data sets (see Wimmer-Schweingruber et al. 2021), we were able to link irregular particle behavior to the plasma irregularities (discontinuities, reconnection) present in the same region, a study in continuity with others using EPD in different environments (e.g., Trotta et al. 2023). On the other hand, it was shown that a significant amount of high-energy ($\sim$7 MeV) particles may be generated in the interaction between weak eruptive events, with important consequences for ongoing modeling efforts in SEP acceleration and propagation (e.g., Ding et al. 2024).

The forward–reverse shock pair propagating in CME material also offers opportunity to study shock microphysics in unusual ambient parameters, as in the case of the forward shock exhibiting an extended particle foreshock despite the very low Mach number, probably due to the low level of upstream magnetic field fluctuations of CME1 (see Trotta et al. 2021; Lario et al. 2022). Studying shock behavior in this poorly explored parameter space is important for the astrophysical implications of this research, and will be the object of further studies.

This study exploited the unique orbital configuration during the event, with two remote CME candidates identified using STEREO-A and near-Earth observers. These are compatible with CME1 being a faint eruption, originating from AR 12957, then interacting with CME2, which is more energetic and originating from AR 12958, as shown by the time–elongation maps in Figure 3. Despite the large uncertainties involved, GCS fits yield CME propagation speeds compatible with this scenario. These observations highlighted the importance of connecting remote and direct observations, particularly due to CME1 being particularly faint and slow, yet giving rise to such an interesting event.

We also investigated the evolution of this structure at 1 au using the Wind spacecraft, revealing a merged structure without a forward–reverse shock pair and mixed features between a CME and SIR event. At 1 au, the structure became a moderate event, common around solar maximum, underlining that without an inner heliosphere upstream observer we would have little knowledge of its origins and evolution. This is in contrast with SIR-related shock pairs, which get more intense with heliospheric distance. The fact that such CME–CME-related shock pairs seem to weaken with heliocentric distance is compatible with the fact that they have not been identified previously and with earlier simulation studies of interacting CMEs (Lugaz et al. 2005).

Obtaining further insight into the evolution of these transient, complex interactions has relevant implications to space weather events (Möstl et al. 2020) and will be further investigated exploiting the extended spacecraft fleet orbiting the inner heliosphere.

Acknowledgments

This study has received funding from the European Union's Horizon 2020 research and innovation program under grant agreement No. 101004159 (SERPENTINE, www.serpentine-h2020.eu). Views and opinions expressed are, however, those of the authors only and do not necessarily reflect those of the European Union or the European Research Council Executive Agency. Neither the European Union nor the granting authority can be held responsible for them. This work was supported by the UK Science and Technology Facilities Council (STFC) grant ST/W001071/1. Solar Orbiter magnetometer operations are funded by the UK Space Agency (grant ST/X002098/1). Solar Orbiter is a space mission of international collaboration between ESA and NASA, operated by ESA. Solar Orbiter Solar Wind Analyser (SWA) data are derived from scientific sensors which have been designed and created, and are operated under funding provided in numerous contracts from the UK Space Agency (UKSA), the UK Science and Technology Facilities Council (STFC), the Agenzia Spaziale Italiana (ASI), the Centre National d'Etudes Spatiales (CNES, France), the Centre National de la Recherche Scientifique (CNRS, France), the Czech contribution to the ESA PRODEX program and NASA. Solar Orbiter SWA work at UCL/MSSL is currently funded under STFC grants ST/W001004/1 and ST/X/002152/1. The Energetic Particle Detector (EPD) on Solar Orbiter is supported by the Spanish Ministerio de Ciencia, Innovación y Universidades FEDER/MCIU/AEI Projects ESP2017-88436-R and PID2019-104863RB-I00/AEI/10.13039/501100011033 and the German space agency (DLR) under grant 50OT2002. X.B.-C. is supported by DGAPA-PAPIIT grant IN106724. H.H. is supported by the Royal Society University Research Fellowship URF\R1\180671. N.F. is supported by the UKRI/STFC grant ST/W001071/1. A.L. and O.P. are supported by the PRIN 2022 project "2022KL38BK—The ULtimate fate of TuRbulence from space to laboratory plAsmas (ULTRA)" (Master CUP B53D23004850006) by the Italian Ministry of University and Research, funded under the National Recovery and Resilience Plan (NRRP), Mission 4—Component C2—Investment 1.1, "Fondo per il Programma Nazionale di Ricerca e Progetti di Rilevante Interesse Nazionale (PRIN 2022)" (PE9) by the European Union—NextGenerationEU. A.L. also acknowledges the support of the STFC Consolidated grant ST/T00018X/1. E.P. acknowledges support from NASA's Heliophysics Guest Investigators-Open program (grant No. 80NSSC23K0447). S.W.G. is supported by the Research Council of Finland (INERTUM, grant No. 346612). E.Y. is supported by Swedish National Space Agency (grant No. 192/20). N.D. acknowledges the support by the Research Council of Finland (SHOCKSEE, grant No. 346902).

T.S.H. is supported by STFC grant ST/W001071/1. Note that we used the RTN coordinate system throughout this work, routinely used for heliospheric missions. However, transformations

to other systems of coordinates may be performed using the SPICE kernels available at https://www.cosmos.esa.int/web/spice/solar_orbiter for Solar Orbiter and at https://naif.jpl.nasa.gov/naif/ for Wind and STEREO.

ORCID iDs

Domenico Trotta https://orcid.org/0000-0002-0608-8897
Andrew P. Dimmock https://orcid.org/0000-0003-1589-6711
Xochitl Blanco-Cano https://orcid.org/0000-0001-7171-0673
Robert J. Forsyth https://orcid.org/0000-0003-2701-0375
Heli Hietala https://orcid.org/0000-0002-3039-1255
Naïs Fargette https://orcid.org/0000-0001-6308-1715
Andrea Larosa https://orcid.org/0000-0002-7653-9147
Noé Lugaz https://orcid.org/0000-0002-1890-6156
Erika Palmerio https://orcid.org/0000-0001-6590-3479
Simon W. Good https://orcid.org/0000-0002-4921-4208
Juska E. Soljento https://orcid.org/0000-0003-2495-8881
Emilia K. J. Kilpua https://orcid.org/0000-0002-4489-8073
Emiliya Yordanova https://orcid.org/0000-0002-9707-3147
Oreste Pezzi https://orcid.org/0000-0002-7638-1706
Georgios Nicolaou https://orcid.org/0000-0003-3623-4928
Timothy S. Horbury https://orcid.org/0000-0002-7572-4690
Rami Vainio https://orcid.org/0000-0002-3298-2067
Nina Dresing https://orcid.org/0000-0003-3903-4649
Christopher J. Owen https://orcid.org/0000-0002-5982-4667
Robert F. Wimmer-Schweingruber https://orcid.org/0000-0002-7388-173X

References

Belcher, J. W. 1971, ApJ, 168, 509
Chen, P. F. 2011, LRSP, 8, 1
Dimmock, A. P., Rosenqvist, L., Hall, J. O., et al. 2019, SpWea, 17, 989
Ding, Z., Li, G., Wijsen, N., Poedts, S., & Yao, S. 2024, ApJL, 964, L8
Domingo, V., Fleck, B., & Poland, A. I. 1995, SoPh, 162, 1
Dresing, N., Rodríguez-García, L., Jebaraj, I. C., et al. 2023, A&A, 674, A105
Fargette, N., Lavraud, B., Rouillard, A. P., et al. 2023, A&A, 674, A98
Fox, N. J., Velli, M. C., Bale, S. D., et al. 2016, SSRv, 204, 7
Fränz, M., & Harper, D. 2002, P&SS, 50, 217
Gosling, J. T., Bame, S. J., Smith, E. J., & Burton, M. E. 1988, JGR, 93, 8741
Horbury, T. S., O'Brien, H., Carrasco Blazquez, I., et al. 2020, A&A, 642, A9
Howard, R. A., Moses, J. D., Vourlidas, A., et al. 2008, SSRv, 136, 67
Jian, L., Russell, C. T., Luhmann, J. G., & Skoug, R. M. 2006, SoPh, 239, 337
Kaiser, M. L., Kucera, T. A., Davila, J. M., et al. 2008, SSRv, 136, 5
Kilpua, E., Koskinen, H. E. J., & Pulkkinen, T. I. 2017, LRSP, 14, 5
Kilpua, E. K., Lumme, E., Andreeova, K., Isavnin, A., & Koskinen, H. E. 2015, JGRA, 120, 4112
Laker, R., Horbury, T. S., O'Brien, H., et al. 2024, SpWea, 22, e2023SW003628
Lario, D., Richardson, I. G., Wilson, L. B. I., et al. 2022, ApJ, 925, 198
Lepping, R. P., Acũna, M. H., Burlaga, L. F., et al. 1995, SSRv, 71, 207
Lin, R. P., Anderson, K. A., Ashford, S., et al. 1995, SSRv, 71, 125
Lugaz, N., & Farrugia, C. J. 2014, GeoRL, 41, 769
Lugaz, N., Manchester, W. B. I., & Gombosi, T. I. 2005, ApJ, 634, 651
Lugaz, N., Temmer, M., Wang, Y., & Farrugia, C. J. 2017, SoPh, 292, 64
Möstl, C., Weiss, A. J., Bailey, R. L., et al. 2020, ApJ, 903, 92
Müller, D., St, Cyr, O. C., Zouganelis, I., et al. 2020, A&A, 642, A1
Nakagawa, T., Nishida, A., & Saito, T. 1989, JGR, 94, 11761
Ogilvie, K. W., & Desch, M. D. 1997, AdSpR, 20, 559
Ogilvie, K. W., Chornay, D. J., Fritzenreiter, R. J., et al. 1995, SSRv, 71, 55
Owen, C. J., Bruno, R., Livi, S., et al. 2020, A&A, 642, A16
Palmerio, E., Kilpua, E. K. J., & Savani, N. P. 2016, AnGeo, 34, 313
Palmerio, E., Nieves-Chinchilla, T., Kilpua, E. K. J., et al. 2021a, JGRA, 126, e2021JA029770
Palmerio, E., Nitta, N. V., Mulligan, T., et al. 2021b, FrASS, 8, 695966
Pesnell, W. D., Thompson, B. J., & Chamberlin, P. C. 2012, SoPh, 275, 3
Rice, W. K. M., Zank, G. P., & Li, G. 2003, JGRA, 108, 1369
Richardson, I. G. 2018, LRSP, 15, 1
Richardson, J. D., Burlaga, L. F., Elliott, H., et al. 2022, SSRv, 218, 35
Rodríguez-Pacheco, J., Wimmer-Schweingruber, R. F., Mason, G. M., et al. 2020, A&A, 642, A7
Russell, C. T., Priest, E. R., & Lee, L. C. 1990, Physics of Magnetic Flux Ropes (Washington, DC: American Geophysical Union), 58
Schwenn, R. 1996, Ap&SS, 243, 187
Scolini, C., Chané, E., Temmer, M., et al. 2020, ApJS, 247, 21
Temmer, M. 2021, LRSP, 18, 4
Temmer, M., Reiss, M. A., Nikolic, L., Hofmeister, S. J., & Veronig, A. M. 2017, ApJ, 835, 141
Thernisien, A. 2011, ApJS, 194, 33
Trotta, D., Horbury, T. S., Lario, D., et al. 2023, ApJL, 957, L13
Trotta, D., Larosa, A., Nicolaou, G., et al. 2024, ApJ, 962, 147
Trotta, D., Valentini, F., Burgess, D., & Servidio, S. 2021, PNAS, 118, e2026764118
Trotta, D., Vuorinen, L., Hietala, H., et al. 2022, FrASS, 9, 1005672
Verbeke, C., Mays, M. L., Kay, C., et al. 2023, AdSpR, 72, 5243
Wimmer-Schweingruber, R. F., Janitzek, N. P., Pacheco, D., et al. 2021, A&A, 656, A22
Zhang, J., Richardson, I. G., Webb, D. F., et al. 2007, JGRA, 112, A10102
Zhuang, B., Lugaz, N., Gou, T., Ding, L., & Wang, Y. 2020, ApJ, 901, 45
Zurbuchen, T. H., Weberg, M., von Steiger, R., et al. 2016, ApJ, 826, 10